# Can a Hand-Held 3D Scanner Capture Temperature-Induced Strain of Mortar Samples? Comparison between Experimental Measurements and Numerical Simulations

Alexander Haynack [1,*,†], Sekandar Zadran [2,*,†], Jithender J. Timothy [1], Serena Gambarelli [2], Thomas Kränkel [1], Charlotte Thiel [3], Joško Ožbolt [2] and Christoph Gehlen [1]

1    Centre for Building Materials (CBM), Chair of Materials Science and Testing,
     Department of Materials Engineering, TUM School of Engineering and Design,
     Technical University of Munich, 81245 Munich, Germany
2    Materials Testing Institute (MPA), University of Stuttgart, 70569 Stuttgart, Germany
3    Civil Engineering Faculty, OTH Regensburg, 93053 Regensburg, Germany
*    Correspondence: alexander.haynack@tum.de (A.H.); zadran.sekander@mpa.uni-stuttgart.de (S.Z.)
†    These authors contributed equally to this work.

**Abstract:** The expected lifespan of cement-based materials, particularly concrete, is at least 50 years. Changes in the pore structure of the material need to be considered due to external influences and associated transport processes. The expansion behaviour of concrete and mortar during freeze–thaw attacks, combined with de-icing salt agents, is crucial for both internal and external damage. It is essential to determine and simulate the expansion behaviour of these materials in the laboratory, as well as detect the slow, long-term expansion in real structures. This study measures the expansion of mortar samples during freeze–thaw loading using a high-resolution hand-held 3D laser scanner. The specimens are prepared with fully or partially saturated pore structures through water storage or drying. During freeze–thaw experiments, the specimens are exposed to pure water or a 3% sodium chloride solution (NaCl). Results show contraction during freezing and subsequent expansion during thawing. Both test solutions exhibit similar expansion behaviour, with differences primarily due to saturation levels. Further investigations are required to explore the changing expansion behaviour caused by increasing microcracking resulting from continuous freeze–thaw cycles. A numerical analysis using a 3D coupled hygro-thermo-mechanical (HTM) model is conducted to examine the freeze–thaw behaviour of the mortar. The model accurately represents the freezing deformation during the freeze–thaw cycle.

**Keywords:** concrete; mortar; durability; freeze–thaw and de-icing salt resistance; strain; 3D laser scanning; numerical simulation; 3D FE numerical model; hygro-thermo-mechanical coupling

**MSC:** 7405; 74S05

## 1. Introduction

Recent design recommendations for concrete structures take into account the environmental cost of the production of building materials and the impact of construction on nature [1]. Hence, the aim is to achieve the highest possible lifespan of buildings. Infrastructure such as bridges is designed for a service life of 100 years [2]. Therefore, durability is a leading consideration in concrete project stages and construction. However, one of the most significant causes of decreased service life for concrete structures in countries with sub-zero temperatures is deterioration caused by freeze–thaw cycles (FTC), with and without the use of de-icing salts. Two types of damage can occur in concrete structures subjected to FTC: scaling from the surface of the concrete and internal damage in the form of microcracks [3]. Requirements for such forms of damage are moisture and ion absorption

as well as moisture and ion redistribution in the material. These transport processes depend on the distribution, amount, type, size, and shape of the capillary pores in the concrete [4]. The pores are caused by surplus water, which is not required for the hydration of the fresh concrete and is therefore bound neither chemically nor physically. The resulting capillary pore structure allows ingress of gases and liquids into the concrete [5]. Durability assessment of concrete is based on selecting a test that replicates the environmental conditions in which the structure is located. Various standards and recommendations for measuring freeze–thaw resistance exist, including DIN CEN/TS 12390-9:2017-05 [6] or regional guidelines like the recommendation from the Federal Institute of Water Infrastructure in Germany [7]. The strain in concrete during FTC is mainly influenced by thermal gradients within the material and the pore pressure resulting from the freezing and thawing of the water within the pores [8]. Monitoring the strain of concrete is considered a possible method of detecting internal cracking [9,10]. As the deterioration progresses, residual strain starts to accumulate, indicating more significant internal damage. Analyzing the incremental strain can be a reliable approach to assessing concrete damage, making it potentially valuable for monitoring specific areas of real concrete structures exposed to freeze–thaw environments [11]. Monitoring the freeze–thaw induced strain of concrete over an extended period of time can be challenging due to surface deterioration. This causes the detachment of sensors such as strain gauges, which are usually attached to the surface of the concrete [11]. A novel approach to determining the dilatation of concrete using a high resolution 3D scanner (Creaform HandySCAN Black Elite) with an accuracy of 25 μm is used in the proposed work. The presented methodology is based on the surface deterioration evaluation algorithm by Haynack et al. [12]. For this study, specimens are exposed to a freeze–thaw cycle between 20 °C and −20 °C over the course of twelve hours and scanned periodically. The resulting change in length of the specimens is used to determine the temperature-induced strain.

To better understand the involved phenomena and confirm the reliability of the proposed measuring technique, a 3D FE numerical analysis is carried out and the results are compared with the experimental data. A number of models are developed to numerically predict the thermo-mechanical behaviour of porous materials, specifically cement paste, subjected to freeze–thaw action. Powers' hydraulic and osmotic pressure theories formed the basis of freeze–thaw damage theory [13,14]. Bažant et al. established a mathematical model based on pore size distribution and desorption and adsorption isotherms for concrete [15]. Zuber et al. presented a numerical model based on poromechanics and local thermodynamic equilibrium to predict the behaviour of completely saturated cement-based materials subjected to freezing temperatures [16,17]. Yang et al. proposed a micromechanical model to simulate the expansion of cement paste, taking into account thermal dilatation of the matrix and pressure in the pore space [18]. Timothy et al. proposed a multiscale framework for estimating the critical pore pressure required to initiate microcracks during a freeze–thaw exposition of cementitious materials [19]. Despite the models proposed by various researchers, the freezing process in porous materials like concrete still remains a complex topic due to the interaction between heat transfer, moisture, temperature dependent phase change, pore saturation, and deformation. There are only a few studies available in the literature on the coupled thermo-hygro-mechanical behaviour of concrete under freezing conditions. The goal of the numerical part of this study is to use a 3D coupled hygro-thermo-mechanical model implemented in the in-house FE code MASA [20] to investigate the freeze–thaw behaviour of the cement mortars under fully and partially saturated conditions with two different salt concentrations. The mechanical part of the model is based on the microplane theory [21]. The mechanical and non-mechanical processes are coupled using a staggered solution procedure. The model is validated based on the experimental part of this study and is shown to accurately capture the freezing deformation of the cement mortar during a single freeze–thaw cycle.

## 2. Materials and Exposition

The mix design used in this study consists of an Ordinary Portland cement (CEM I 42.5 N (Heidelberg Cement, Burglengenfeld, Germany) according to DIN EN 197-1 [22]) with a w/c ratio of 0.55 and a maximum aggregate size of 2 mm (quarzitic, natural sand (Quarzwerke, Hirschau, Germany)). The grain size distribution of the aggregates can be taken from Table 1.

**Table 1.** Grain size distribution of aggregates.

| Mesh Size (mm) | 0.063 | 0.125 | 0.25 | 0.5 | 1 | 2 |
|---|---|---|---|---|---|---|
| Passing rate (wt.-%) | 0.06 | 0.49 | 19.16 | 48.40 | 75.47 | 100 |

The mix design of the mortar samples is shown in Table 2. No Air-Entraining Agents were used on purpose to increase potential damage, and a w/c of 0.55 was chosen to have a strongly developed capillary pore system.

**Table 2.** Mixture proportions of mortar.

| w/c (-) | Cement (kg/m³) | Water (kg/m³) | Aggregates (kg/m³) |
|---|---|---|---|
| 0.55 | 560 | 308 | 1312 |

Mortar cubes with the dimensions of $15.0 \times 15.0 \times 15.0$ cm³ were produced. The samples were stored in the formwork for 1 day (hardening). After demoulding, the samples were conditioned under water at $20 \pm 2$ °C until a sample age of 7 days (curing). The samples were then sawn into the dimensions $15.0 \times 11.0 \times 7.0$ cm³. Subsequently, the mortar cuboids were stored in a climate chamber with standardized conditions of $20 \pm 2$ °C and $65 \pm 5$% relative humidity for another 21 days until reaching the sample age of 28 days (drying) according to [6,7]. Afterwards, half of the samples stored in water to achieve full capillary saturation. For this, the samples have been weighed consistently until a constant mass has been reached. The process of capillary saturation lasted a total of 140 days, resulting in a total sample age of 168 days. The other half of the samples was placed 5 mm deep into the test liquid (pure water or 3% sodium chloride (NaCl)) for 7 days to achieve partial saturation of the bottom half of the samples. The samples of the 'saturated' preconditioning were tested after a sample age of 168 days, the 'partially saturated' samples were tested after 35 days. Table 3 shows the two variations of sample preconditioning.

**Table 3.** Preconditioning of mortar samples.

| Label | Hardening (d) | Curing (d) | Drying (d) | Capillary Saturation (d) | Water Storage (d) | Total Age (d) |
|---|---|---|---|---|---|---|
| Saturated | 1 | 6 | 21 | - | 140 | 168 |
| Partially saturated | 1 | 6 | 21 | 7 | - | 35 |

After each variation of preconditioning, the samples were placed into either pure water (demineralized) or 3% of sodium chloride. The samples were then stored inside a liquid cooled freeze–thaw chamber with a cyclic temperature exposition between 20 °C and −20 °C over the course of 12 h, see Figure 1, according to the German CDF (Capillary Suction of De-icing chemicals and freeze–thaw) and CIF (Capillary suction, Internal damage and freeze–thaw) tests [6,7]. These tests are mainly used to examine the freeze–thaw resistance (CIF) and freeze–thaw resistance in combination with de-icing salt agents (CDF) in Germany. The main goal of the simulation is to determine both internal and external damage occurring during the CDF test. Prior to that, an integral part of the simulation is to correctly replicate the temperature induced strain behaviour during the freeze–thaw test. Therefore, the FTC depicted in Figure 1 has been chosen.
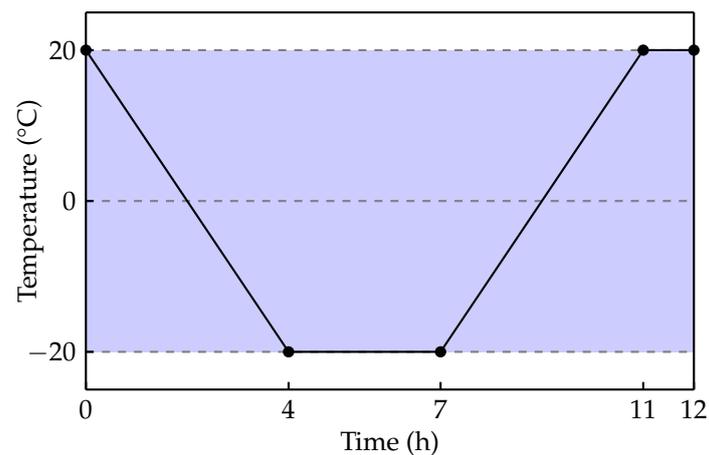
**Figure 1.** Visualization of one freeze–thaw cycle (FTC).

The freezing rate for the first cooling phase was 10 °C/h until the temperature reached a value of −20 °C at the end of the 4th hour. The temperature was then kept constant at −20 °C for three hours followed by the thawing rate of 10 °C/h for four hours until the temperature reached 20 °C. At this point the temperature was kept constant at 20 °C for one hour which marks the end of the freeze–thaw cycle.

Inside the freeze–thaw chamber, the samples are placed in containers with the dimensions of 53.0 × 32.5 × 6.0 cm³. The height of the containers of only 6.0 cm has been chosen to ensure complete visibility of the samples during the scanning process. The test setup is shown in Figure 2. The temperature load is applied by the cooling liquid underneath the containers.
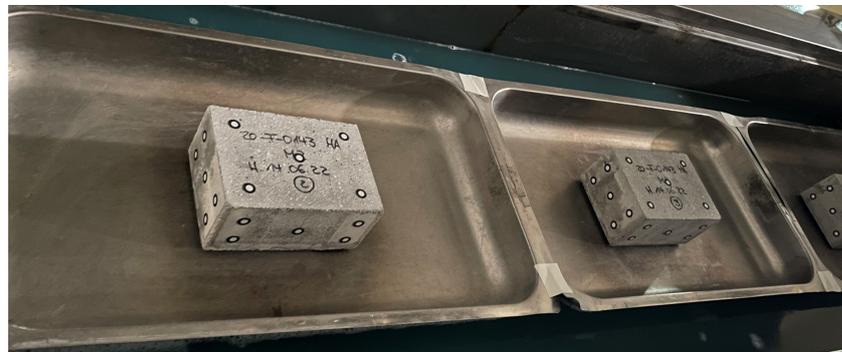


**Figure 2.** Test setup for the strain measurements. Samples are placed inside containers in the freeze–thaw chamber.

## 3. Methods

### 3.1. Three-Dimensional (3D) Scan Data Evaluation

The samples have been examined once every hour over the course of one full FTC. For this, the samples have been scanned with a hand-held 3D scanner (HandySCAN Black Elite by Creaform (Levis, Canada)) with an accuracy of 0.025 mm. The device is shown in Figure 3.

**Figure 3.** Three-dimensional (3D) laser scanner used for the measurement of displacements of the samples during the cyclical freeze–thaw temperature load.

On each side of the specimen, five target markers have been applied, see Figure 4. These are referred to as top left, top right, bottom left, bottom right, and middle. For each timestep, the horizontal and vertical point distances have been determined as seen in Figure 5. The chosen timestep of subsequent strain measurements was 1 h, resulting in a total of 13 measurements during the freeze–thaw cycle.

Ultimately, the strain $\varepsilon$ of each specimen has been determined by referring the change in distance $\Delta l$ after each timestep $t_i$ to the initial distance $l_0$, see Equation (1).

$$\varepsilon = \frac{\Delta l(t_i)}{l_0}. \tag{1}$$



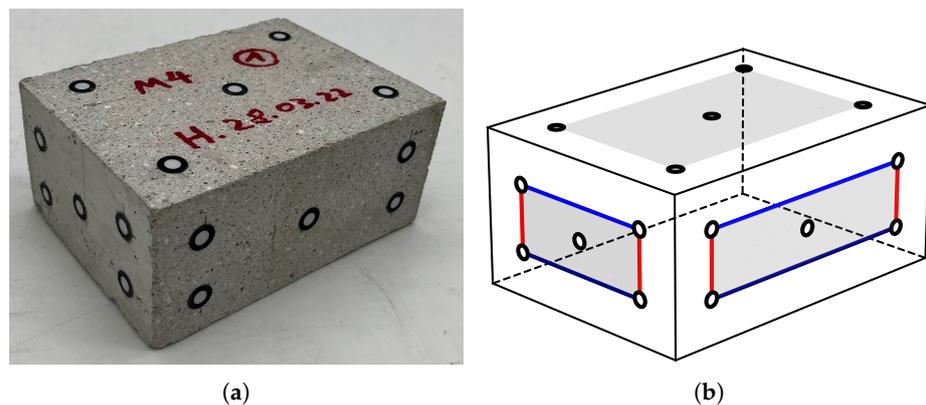(**a**)                                                                 (**b**)

**Figure 4.** Visualization of the applied disc shaped target markers on (**a**) a mortar sample and (**b**) a 3D model of a sample with colored lines representing the strain directions according to Figure 5. Non-visible sides of the specimens also contain target markers.
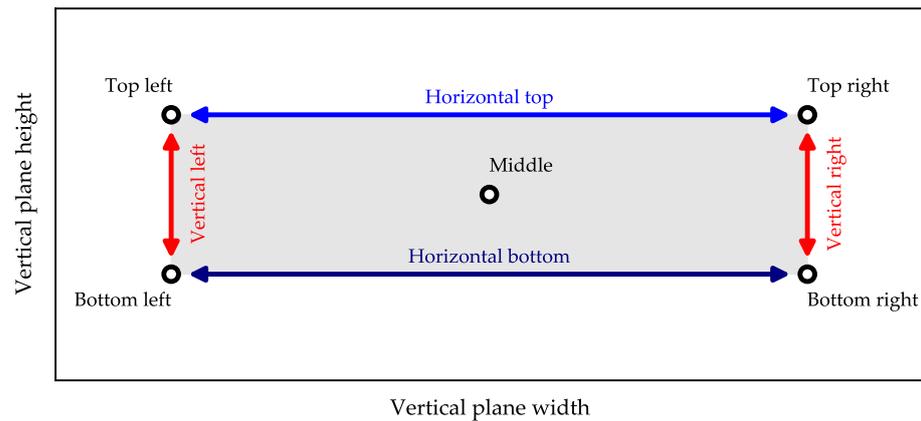
**Figure 5.** Naming and color convention of target markers and strain directions of one exemplary plane of a mortar sample.

*3.2. Numerical Simulation*

3.2.1. Mathematical Formulation of the Model

The mathematical formulation for the freezing process in this study is essentially referred to the model proposed by the authors. The model is very well described in [23] and a summary of the mathematical formulation is presented in this section. A poromechanical approach is used to investigate the freezing behaviour of cementitious materials. The material is considered as a porous medium which is saturated with water/salt solution and subjected to freezing conditions. The constitutive equations for phase change, mass transfer, and heat transfer are set up based on the relevant thermodynamic laws. Consequently, a homogenization scheme is employed to convert the pore pressure induced by freezing into a macroscopic effective stress. The primary governing variables are the water fluid pressure $p_w$ (Pa), temperature $T$ (°C), and strains $\varepsilon$ (-). The constitutive equation for the pressure in the liquid water is given as:

$$\beta \dot{p}_w = \nabla \cdot (\frac{D}{\eta} \nabla p_w) + S - b\dot{\varepsilon}_v, \tag{2}$$

where $D$ = permeability (m²) of the porous media; $p_w$ = pressure in the liquid water (Pa); $\eta$ = fluid viscosity (Pa sec); $\varepsilon_v$ = volumetric strain of the medium (Pa); $b$ = Biot's coefficient (-). $\beta$ is the ratio of proportions of the porosity filled with ice and liquid water to their compressibility moduli and the ratio of Biot's coefficient to the compressibility modulus of the solid matrix. $S$ (Pa) denotes the source of pressure and is composed of four terms.

Based on the Darcy's law, Equation (2) takes into account the coupling between deformation, ice formation, and water and heat transfer.

The differential equation for heat conduction takes the following form:

$$\rho C \dot{T} = \nabla \cdot (\lambda \nabla T) + L \dot{w}_i, \tag{3}$$

where $\rho$ = density of the system (kg/m³); $\lambda$ = thermal conductivity of the system (W/(m K)); $C$ = heat capacity of the system (J/(kg K)); and $L$ = latent heat of fusion of water (kJ/kg). The last term in Equation (3) introduces a coupling between the heat transfer and the phase change and has an appreciable effect on freeze–thaw problems.

The governing equation for the mechanical behaviour of a continuous body in case of static loading is given by:

$$\nabla \cdot (C_m \nabla u) - \nabla p_T - b \nabla p^* + f = 0, \tag{4}$$

where $C_m$ = material stiffness tensor; $u$ = displacement field; $p_T$ = volumetric stress due to free thermal strains of the porous material; $f$ = specific volume load.

The above partial differential equations (Equations (2)–(4)) are first rewritten into a weak form based on the Galerkin weighted residual method. The non-mechanical part of the system, represented by Equation (2), is solved iteratively using the direct integration method of implicit type. The mechanical part of the problem, (Equation (4)) is solved using the Newton–Raphson iterative scheme. The coupling between the mechanical and non-mechanical parts of the model is achieved through the continuous update of governing parameters during the incremental transient finite element analysis, employing a staggered solution scheme.

### 3.2.2. Geometry and FE Discretization

The presented study is carried out based on the experimental work described above to numerically investigate the freeze–thaw behaviour of the specimens under fully and partially saturated conditions. The numerical study is carried out using a 3D coupled hygro-thermo-mechanical model implemented in the in-house FE code MASA [20]. The specimens used in the experimental part of the work have dimensions of $15.0 \times 11.0 \times 7.0$ cm³. Due to double geometric symmetry, only one quarter of the cuboid, indicated by the shadowed section in Figure 6a, is numerically analyzed to save computational time. As shown in Figure 6b, the two shaded faces are the symmetrical faces of the cuboid. The resultant quarter part of the specimen used for numerical simulations has reduced dimensions of $7.5 \times 5.5 \times 7.0$ cm³.

In the presented study, the quarter size cuboid with the same cement paste as investigated in the experiments is numerically analyzed to reproduce the freeze–thaw behaviour of the material under fully and partially saturated conditions with pure water and a 3% NaCl solution. The water–cement ratio, boundary conditions, and freeze–thaw rate were set as in the experiments.
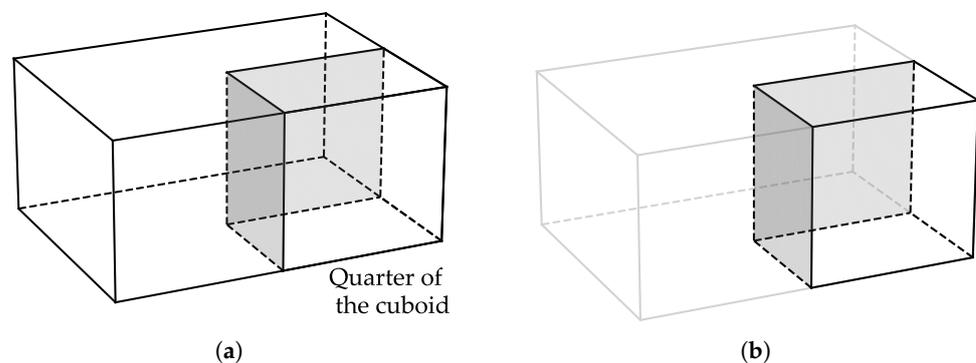


| (a) | (b) |

**Figure 6.** Depiction of the specimen: (**a**) quarter of the cuboid, (**b**) symmetrical face identification.

The FE discretization was performed using 3465 solid eight-node elements (Figure 7). The size of the elements in the vertical direction of the model is selected between 1.5 to 5 mm increasing from the bottom towards the top of the specimen. The non-uniform discretization of the mesh in the vertical direction of the specimen is used to better capture the freezing deformation of cement paste at the bottom part of the specimen (first 10 mm) under partially saturated condition. For partially saturated condition, as performed experimentally, the specimen at the age of 7 days was dried for 21 days under standardized conditions of $20 \pm 2$ °C and $65 \pm 5$ % relative humidity (RH). Following the drying period, the specimen was submerged 5 mm deep in the liquid solution for 7 days. At the end of the capillary saturation, the specimen was subjected to the freeze–thaw cycle (Figure 1). To determine the moisture content distribution of the near-surface concrete, the NMR MOUSE PM25 from Magritek was used. The measurements were carried out with the CPMG pulse sequence (128 echoes, resolution 500 µm, wait time 500 ms, 256 scans, echo time 0.063 ms). Prior to the test, the surface of the samples has been dried and the samples were wrapped in plastic wrap to prevent further drying during the measurements. The NMR results at the end of capillary saturation period showed a moisture content distribution of 10% by

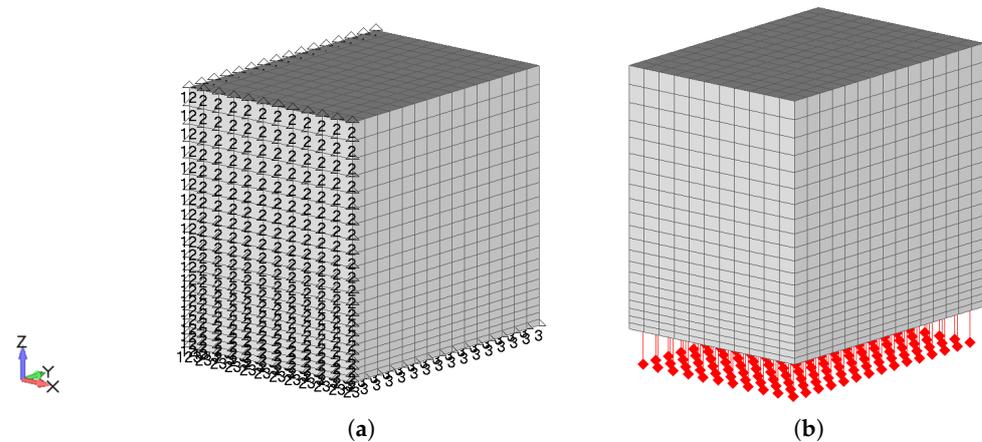mass at the first 9.6 mm of the specimen from the bottom.



**Figure 7.** FE model: (**a**) mechanical boundary condition, (**b**) environmental boundary condition.

The mechanical and environmental boundary conditions of the FE model during the freeze–thaw process are shown in Figure 7. The temperature variation is applied through the bottom surface of the specimen.

To numerically simulate the partially saturated condition, a simplified assumption was made, i.e., the initial RH of the specimen was assumed to be 65%. However, experimentally, the wet specimen was dried for 21 days at $20 \pm 2$ °C and 65% RH before capillary saturation. The exact RH distribution inside the specimen after drying was not known and could not be reproduced numerically. However, the aim was to numerically reach a fully saturated condition for the first 9.6 mm as in the experiment in order to have the same initial condition for the freezing test. Using the adsorption isotherm from [24], the corresponding initial moisture content was derived from the initial RH. The wetting process was then simulated from the bottom surface at 100% RH. The capillary saturation numerically took 36 days until the first 9.6 mm of the specimen reached a saturation degree of 0.92 (Figure 8b). As stated by Fagerlund [25], the critical degree of saturation for cementitious materials may vary from 0.50 to 0.92 depending on the mix proportion, degree of hydration, curing condition, etc. Therefore, this value was calibrated in the model as 0.92 in order to achieve the best fit with the experimental results. It was assumed that, for a water saturation degree (WSD) higher than 0.92, the material can be considered fully saturated.

Model parameters for the numerical analysis of the distribution of RH for 0.55 water–cement ratio are shown in Table 4 [24].

**Table 4.** Used model parameters for the numerical analysis of relative humidity distribution, taken from [24].

| Parameters | w/c = 0.55 |
|:---:|:---:|
| Water vapour permeability, $\rho_v$ (s) | $1.0 \times 10^{-10}$ |
| Surface humidity transf. coeff., $\beta_{hum}$ (m/s) | $2.0 \times 10^{-6}$ |

Figure 8a shows the distribution of relative humidity during the wetting process for 5, 15, 28, and 36 days, respectively. It can be seen that, based on the application of the RH from the bottom surface of the specimen, the distribution of RH is decreasing towards the top of the specimen. As the wetting process continues, the amount of RH inside the specimen increases. The maximum amount of RH after 5 days wetting at the top of the specimen has reached a value of 70%, while this value is 94% after 36 days wetting. Figure 8b represents the water saturation degree inside the specimen based on the distribution of RH. The degree of saturation is determined from the ratio of moisture content and total porosity of the specimen.
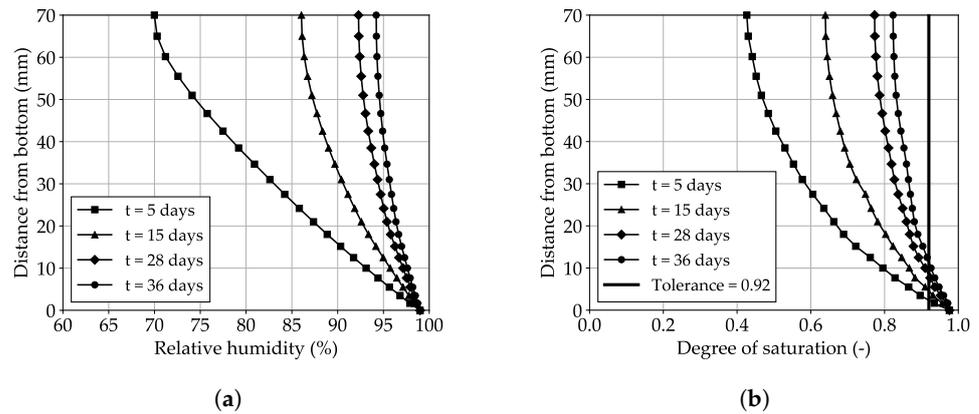
(**a**)　　　　　　　　　　　　　　　　　　　(**b**)

**Figure 8.** (**a**) Distribution of RH across the height, (**b**) obtained degree of saturation during wetting process.

Figure 9 shows a three-dimensional representation of the relative humidity distribution across the specimen for four different wetting periods.
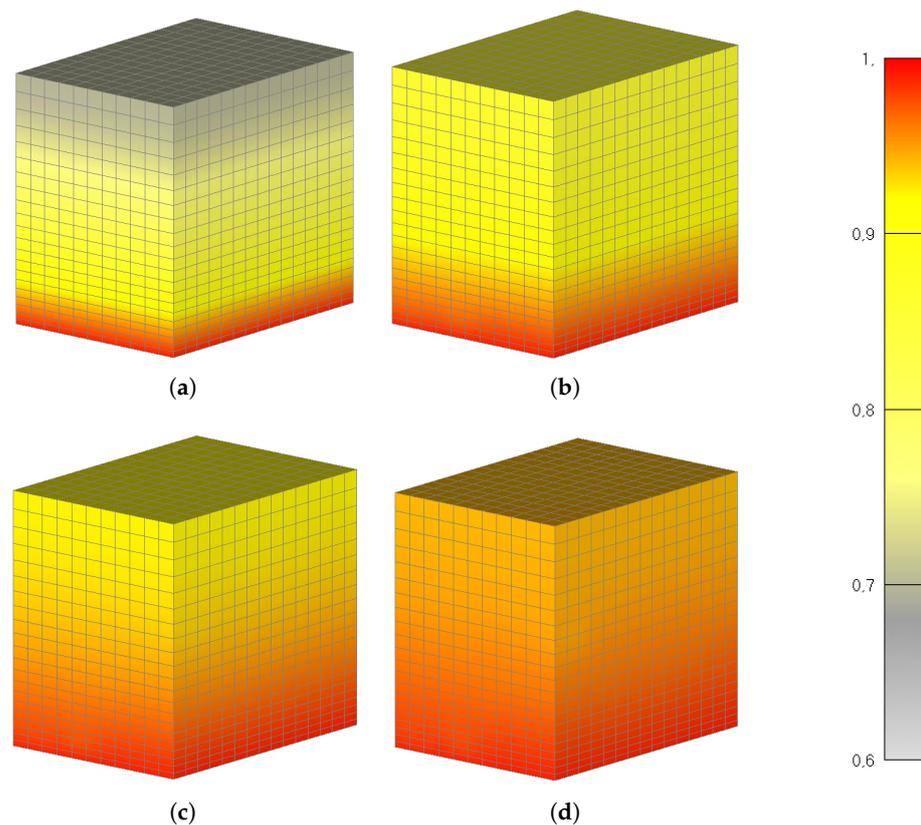


(**a**)　　　　　　　　　　　　　　　　　　　(**b**)

(**c**)　　　　　　　　　　　　　　　　　　　(**d**)

**Figure 9.** Distribution of RH across the section: (**a**) t = 5 days, (**b**) t = 15 days, (**c**) t = 28 days, (**d**) t = 36 days.

The hydraulic pore pressure at the bottom surface of the specimen and the initial hydraulic pressure was set to zero, approximately atmospheric pressure (0.10 MPa).

Analogously to the experiments, the environmental boundary conditions were applied to the bottom surface of the model as heat flux (Figure 7). The time step for the numerical simulation was set to 300 s throughout the full freezing–thawing cycle.

There is a distinction made between two simulation cases. The specimens are exposed to the cyclic temperature load according to Figure 1 and are stored either in pure water (0% NaCl solution) or a 3% NaCl solution.

### 3.2.3. Material Parameters

Input parameters of the porous medium and a solid skeleton of the cement paste are experimentally obtained and reported in Table 5.

**Table 5.** Input material properties of porous medium and solid skeleton of the cementitious matrix.

| Property | Symbol | Unit | Value | Reference Source |
|---|---|---|---|---|
| Apparent density | $\rho$ | (g/cm³) | 2.5 | Experiment |
| Poisson's ratio | $\nu$ | - | 0.18 | Literature [23] |
| w/c | - | - | 0.55 | Experiment |
| Total porosity | $n$ | (m³/m³) | 0.17 Figure 10 | Experiment |
| Elastic modulus | $E$ | (GPa) | 30 | Experiment |
| Compressibility modulus of the porous skeleton | $K_0$ | (GPa) | $E/3(1-2\nu)$ | Literature [23] |
| Compressibility modulus of the solid matrix | $K_m$ | (GPa) | $K_0/(1-n)^3$ | Literature [23] |
| Biot's coefficient | $b$ | - | $1-K_0/K_m$ | Literature [23] |
| Pore size distribution | - | (-) | Figure 10 | Experiment |
| Thermal conductivity | $\lambda_m$ | (W/m*K) | 2.5 | Experiment |
| Heat capacity | $C_m$ | (J/kg*K) | 937.0 | Experiment |
| Thermal expansion coefficient | $\alpha$ | (°C$^{-1}$) | $1.64 \times 10^{-5}$ | Literature [26] |
| Liquid water permeability | $D$ | (m²) | Saturated: $6.0 \times 10^{-18}$<br><br>Partially Saturated:<br>WSD $\geq$ 0.92:<br>$3.17 \times 10^{-17}$<br>0.92 > WSD > 0.80:<br>$1.58 \times 10^{-17}$<br>WSD $\leq$ 0.80:<br>$1.26 \times 10^{-17}$ | Literature [27] |

The parameter of liquid water permeability was calibrated such that the freezing strains best fit the experimental results for a fully saturated condition. The calibrated value of the liquid water permeability is in a reasonable range with the experimental and numerical values reported in [27] for fully saturated conditions. The available experimental and numerical data on the value of liquid water permeability for cement pastes show that this parameter varies significantly ($10^{-23}$ m² to $10^{-17}$ m²). The pore structure and pore size distribution of the material, the degree of saturation, and the chosen experimental and numerical methodologies can be attributed to this variation.

For partially saturated conditions, the value of liquid water permeability is implemented as a function of the water saturation degree of the cement paste. As stated earlier, the freezing process for the current study in a partially saturated condition takes place at a WSD of 0.92 and higher. Based on Figure 8b, the saturation degree of the specimen after 36 days wetting varies between 0.80 to 1.00. Therefore, to take into account the freezing process for different levels of saturation, the parameter of liquid water permeability is extracted from [27] and is shown in Table 5. As shown in [27], the value of liquid water permeability is directly proportional to the water saturation degree in a partially saturated condition. Generally, when the water saturation degree decreases, the number of connected pores that are filled with water decreases, which reduces the number of pathways for water transport in the system. Additionally, the bigger pores are the first to dry up, which further reduces permeability [28].

The coefficient of thermal expansion for the cement paste is calculated based on the total porosity of cement paste provided in [26], see Equation (5).

$$\alpha_d = \alpha_c(1 - n)^{2.66} \tag{5}$$

with $\alpha_c = 26.98 \times 10^{-6}/°C$.

The pore size distribution (PSD) curve used in the model was experimentally obtained for the cement paste using the mercury intrusion porosimetry (MIP) method and is shown in Figure 10. In this measurement method, mercury is gradually pressed into the material as the pressure increases. At each pressure step, the volume of the penetrated mercury is measured. The intrusion volume of the mercury can be converted into a pore size distribution based on the linear relationship between pressure and pore size according to the Washburn equation [29]. Due to the non-wetting contact angle between mercury and the material, increasing pressure is required for penetration into pores with smaller radii [30]. In preparation for the MIP measurements, approximately 3–6 mm-sized pieces are mechanically broken out from the specimens near the surface and dried in a vacuum oven at 40 °C for 24 h.
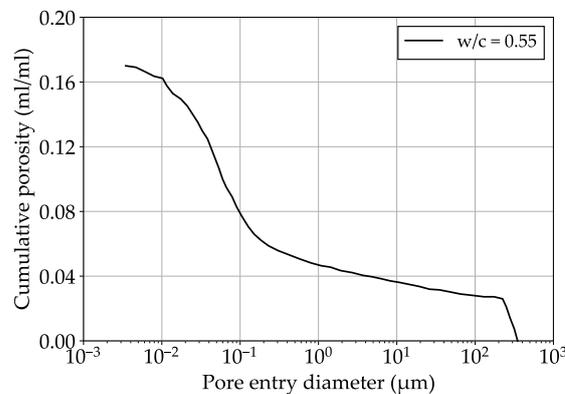


**Figure 10.** Pore size distribution of the cement paste.

## 4. Results and Discussion

### 4.1. General

To examine the raw data of scanned target markers at the most significant areas of the samples, four different directions of target marker displacement were chosen—the horizontal displacement of the vertical surface areas at the (a) top and the (b) bottom of the sample, the (c) vertical displacement of the left and right target markers of each vertical plane, as well as the displacement (d) through the sample along the axis direction, see Figure 11. The target markers on the back sides of the specimens, which are not shown in Figure 11, are also considered in the evaluation of the strain values. Similar to the experimental setup, the horizontal and vertical displacements of the selected target markers are numerically obtained from the corresponding nodal displacements.

The displacement values depicted in Figure 11 are used for the determination of the subsequent strain values.
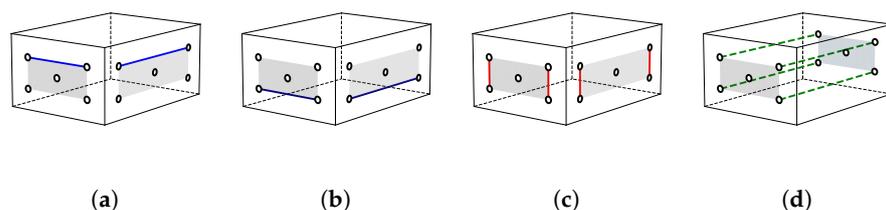


(**a**)　　　　　　　　(**b**)　　　　　　　　(**c**)　　　　　　　　(**d**)

**Figure 11.** Overview of strain value determination: displacement of target markers at the (**a**) horizontal top, (**b**) horizontal bottom, (**c**) vertical, and (**d**) through the sample.

Table 6 provides an overview of the boundary conditions for the different subfigures of the subsequent strain figures. Samples for both types of preconditioning (saturated and partially saturated) have been exposed to both test solutions (NaCl and pure water), resulting in four different variations of boundary conditions.

**Table 6.** Overview of boundary conditions of subfigures in subsequent strain figures.

| Variation | Test Solution | Preconditioning |
|-----------|---------------|-----------------|
| V1 | NaCl | Saturated |
| V2 | NaCl | Partially saturated |
| V3 | Pure water | Saturated |
| V4 | Pure water | Partially saturated |

For each boundary condition, according to Table 6, all samples showed contraction during freezing and expansion back to the initial state during thawing. Additionally, the contraction during freezing showed a smaller standard deviation compared to the increased variance during thawing. This can be explained by the formation of condensation on the target markers. Due to the negative temperatures of the specimen, the condensation freezes and causes inaccuracies of the measurements.

The standard deviations displayed in Figures 13–15 were determined by considering the corresponding distances (horizontal top, horizontal bottom, or vertical) of each vertical plane of the sample.

The measured and simulated temperatures in the center of the specimens conditioned by the temperature load of the FTC applied at the bottom of the specimens can be seen in Figure 12. These measurements have been performed on separate specimens used for the calibration of the simulation model. From the numerical point of view, the initial temperature within the specimen was set to 20 °C and the measured temperature at the middle of the specimen shows a delay, which is consistent considering the time required for the temperature to transfer towards the top of the specimen. Overall, the experimental and numerical results in terms of temperature distribution across the specimen show a very good agreement.
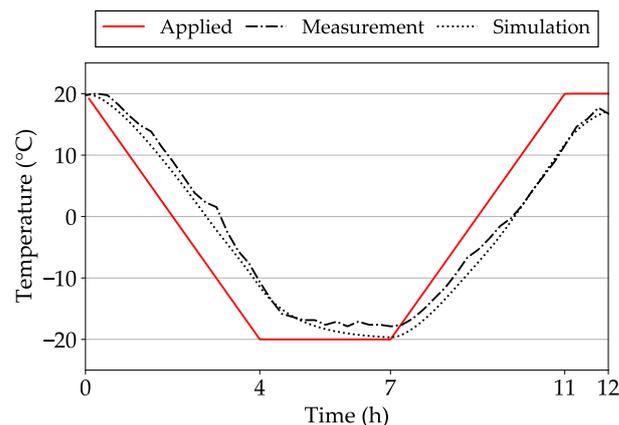


**Figure 12.** Applied temperature on the bottom of the samples, measured and simulated temperatures in the center of the samples.

### 4.2. Horizontal Strain

Figure 13 shows the horizontal strain of the top area of the vertical planes for both the saturated and partially saturated type of preconditioning and for both test solutions (3% NaCl solution and pure water). While showing an overall contraction throughout the freeze–thaw cycle, the simulation data show a minimal expansion at the start of the freezing phase between 0 and −10 °C. For pure water, this expansion appears to be higher compared to the NaCl exposition. The reason for this difference can be attributed to the

different equation for the calculation of the equilibrium pore radius during freezing for pure water compared to the one used for the chloride case. For the case of NaCl solution, the equation takes into account the activity of water in terms of chloride concentration. Since the freezing process is delayed, a similar freezing deformation cannot be expected between the pure water case and the one with chloride. The experimental data do not show any expansion at the start of the freezing phase. Due to the fact that there were only 13 measurements throughout the complete FTC, the duration between each measurement results in one hour. The simulations show that the duration of the expansions caused by the freezing process is less than one hour; therefore, a more detailed measurement of the freezing behaviour could not be performed by the scanning method. Overall, the measurement and simulation data show a similar strain behaviour. For both types of preconditioning, the maximum contraction for the partially saturated samples appears to be higher compared to the saturated samples. Due to a complete capillary saturation of the specimens, the saturated specimens have water occupying all pores, which leads to more freezing and reducing the overall contraction of the material. On the other hand, in a partially saturated condition, the empty pores provide empty space for ice to grow, resulting in a higher contraction.
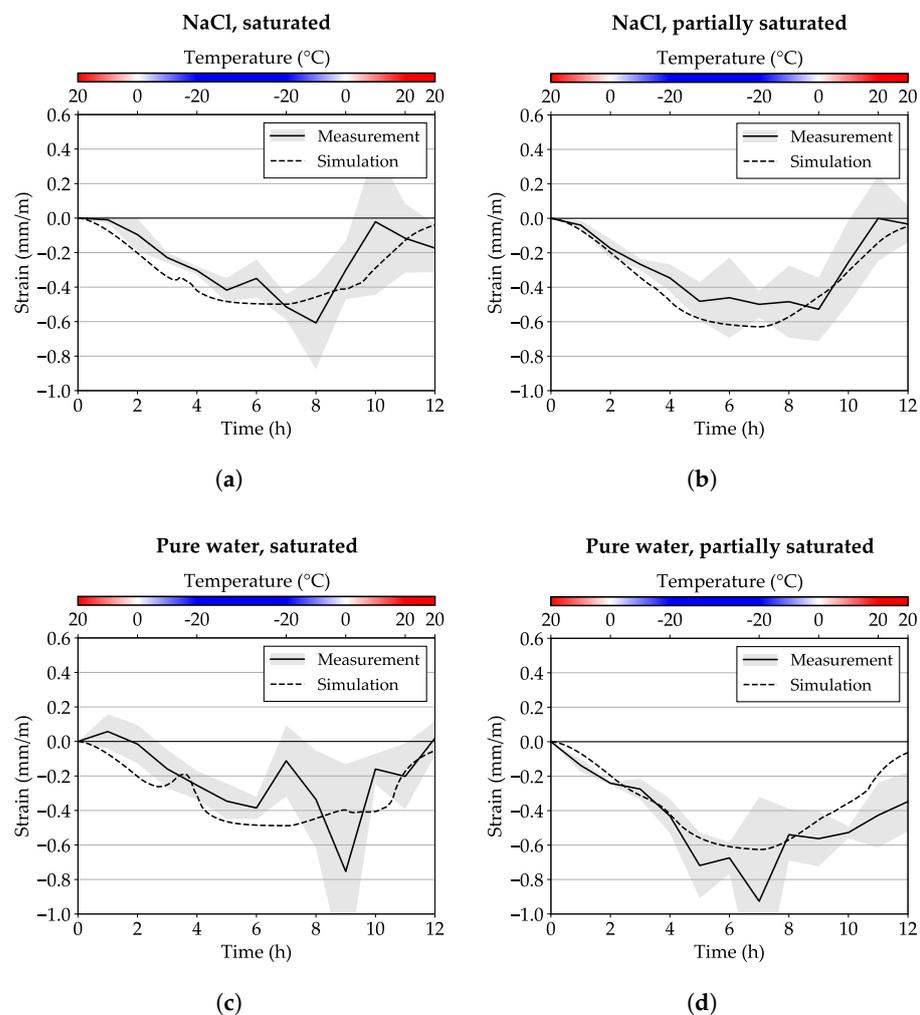


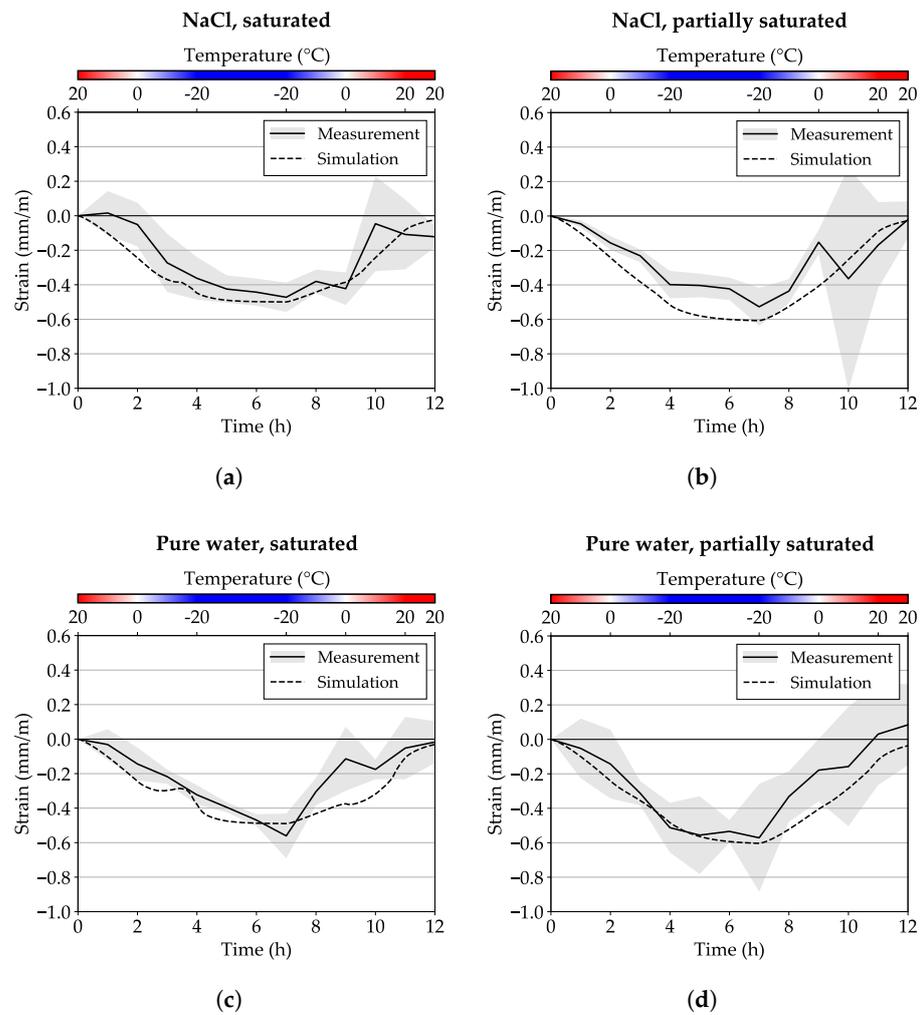**Figure 13.** Horizontal negative values of the axes do infact have minus signs and not hyphens. strain of the top area of the vertical planes, boundary conditions (**a**) V1, (**b**) V2, (**c**) V3, and (**d**) V4 according to Table 6.

Figure 14 shows the horizontal strain of the bottom area of the vertical planes for both the saturated and partially saturated type of preconditioning and for both test solutions (3%

NaCl solution and pure water). The overall strain behaviour can be compared to the top area of the specimens. The simulation data show a reduced slope of contraction during the cooling and freezing phase for the partially saturated samples. This can also be explained by the capillary saturation of the bottom area of the samples allowing higher displacements compared to the empty pore system in the top area of the samples. The fully saturated samples do not show this behaviour due to the even pore saturation through the entire height of the samples.



(**a**)



(**b**)



(**c**)



(**d**)

**Figure 14.** Horizontal strain of the bottom area of the vertical planes, boundary conditions (**a**) V1, (**b**) V2, (**c**) V3, and (**d**) V4 according to Table 6.

## 4.3. Vertical Strain

For both measurements and simulations, the vertical strain of both types of preconditioning and test solution indicates slightly higher values compared to the horizontal strain. Measurements and simulation show a good agreement. Analogous to the horizontal strain values, the partially saturated samples showed a higher maximum contraction compared to the saturated samples. This could be observed for both exposure conditions, see Figure 15.
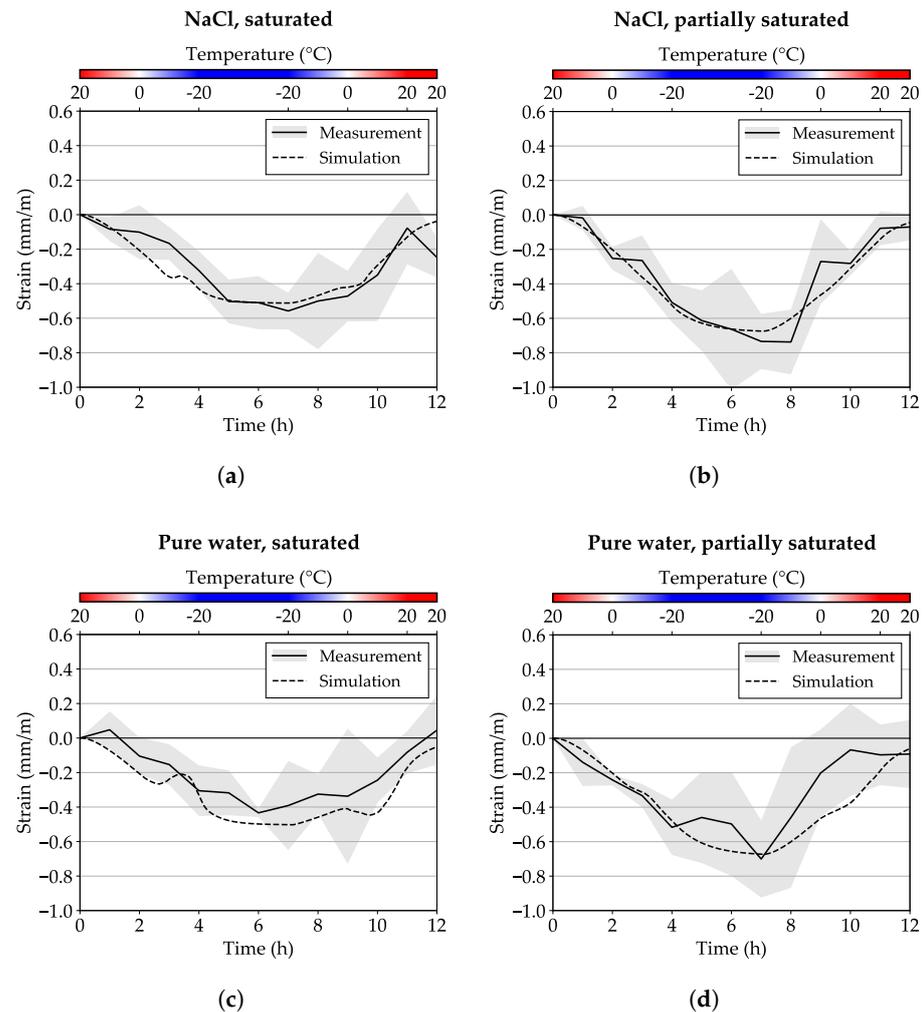
**Figure 15.** Vertical strain of the specimens, boundary conditions (**a**) V1, (**b**) V2, (**c**) V3, and (**d**) V4 according to Table 6.

### 4.4. Strain through the Sample

With the usual approach of using strain gauges for the determination of strains, we are only able to observe the displacements of the surface areas of the samples. The presented methodology also allows for the determination of strain values through the volume of the sample along an axis direction. This can be achieved by measuring the displacements of the target markers of two opposing vertical planes, see Figure 11d).

Figure 16 shows the strain through the specimens along the long axis for both the saturated and partially saturated types of preconditioning and for both test solutions (3% NaCl solution and pure water). It can be observed that the strain values through the sample qualitatively correspond to the behaviour of the 'in-plane' strain. As for the experiments, the numerical results are reported in Figure 16, which show a good agreement with the experimental results.

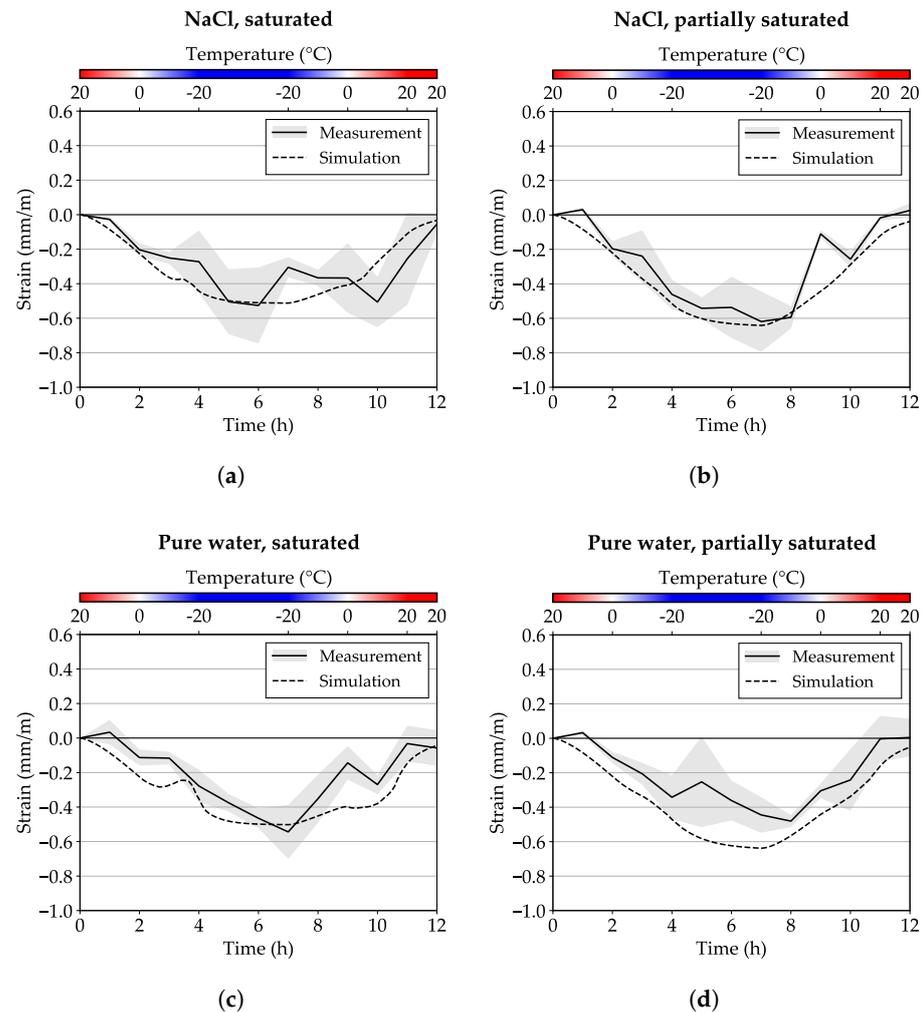Overall, the novel methodology delivers comparable results to the literature data [11].

**Figure 16.** Horizontal strain through the specimens along the axis direction, boundary conditions (**a**) V1, (**b**) V2, (**c**) V3, and (**d**) V4 according to Table 6.

## 5. Conclusions

- Saturated samples show a maximum contraction of $-0.4$ mm/m and partially saturated show a maximum contraction of $-0.6$ mm/m.
- There are certain limitations of the methodology:
  - The methodology is very time consuming due to the fact that the strain measurements are conducted manually.
  - Surface effects (freezing of condensated water on the surface) have an influence on the results.
- Comparing the measurement and simulation results, we can generally observe a similar trend of strain behaviour. The results of the thawing phase usually show the most differences. This can be explained by the aforementioned surface effects.
- The 3D-coupled hygro-thermo-mechanical (HTM) model used in this study is capable of reproducing the freezing behaviour of cementitious material in terms of deformation and heat transfer. The model is validated in [23] as well as based on the experimental results presented here. The key calibration parameters are the liquid water permeability, porosity, pore size distribution, and degree of saturation. These parameters play a significant role in the liquid pressure and freezing deformation of the cement paste. Decreasing the liquid water permeability results in higher liquid pressure and consequent deformation.

To determine the effect of internal damage on the strain behaviour of the samples, multiple measurement cycles need to be performed throughout multiple FTCs. This will be carried out in follow-up investigations.

# References

1. de Brito, J.; Kurda, R. The past and future of sustainable concrete: A critical review and new strategies on cement-based materials. *J. Clean. Prod.* **2021**, *281*, 123558. [CrossRef]
2. Federation internationale du beton. *Fib Model Code for Concrete Structures 2010*; Wilhelm Ernst & Sohn Verlag fur Architektur und technische Wissenschaften: Berlin, Germany, 2013.
3. Stark, J.; Wicht, B. Frost- und Frost-Tausalz-Widerstand von Beton. In *Dauerhaftigkeit von Beton*; Springer: Berlin/Heidelberg, Germany, 2013; pp. 399–471. [CrossRef]
4. Palecki, S. *Hochleistungsbeton unter Frost-Tau-Wechselbelastung:-Schädigung- und Transportmechanismen*; Cuvillier Verlag: Göttingen, Germany, 2005.
5. Powers, T.C.; Copeland, L.E.; Mann, H. *Capillary Continuity or Discontinuity in Cement Pastes*; Technical Report; Portland Cement Association: Washington, DC, USA , 1959.
6. *German Version CEN/TS 12390-9:2016*; Testing Hardened Concrete—Part 9: Freeze–thaw Resistance with De-Icing Salts—Scaling. Beuth Verlag: Berlin, Germany, 2017.
7. *BAW-Merkblatt Frostprüfung von Beton (MFB)*; Merkblatt; Bundesanstalt für Wasserbau: Karlsruhe, Germany, 2012.
8. Şahin, R.; Taşdemir, M.A.; Gül, R.; Çelik, C. Optimization Study and Damage Evaluation in Concrete Mixtures Exposed to Slow Freeze–Thaw Cycles. *J. Mater. Civ. Eng.* **2007**, *19*, 609–615. [CrossRef]
9. Mao, J.; Ayuta, K. Freeze–thaw resistance of lightweight concrete and aggregate at different freezing rates. *J. Mater. Civ. Eng.* **2008**, *20*, 78–84. [CrossRef]
10. Dombrowski, K.I.; Erfurt, W.; Janssen, D. Identifying D-cracking susceptible aggregates-a comparison of testing procedures. In *Proceedings Frost Damage in Concrete*; RILEM Publications s.a.r.l.: Cachan, France, 2002 ; pp. 221–232.
11. Romero, H.; Enfedaque, A.; Gálvez Ruíz, J.C.; Casati, M. *Complementary Testing Techniques Applied to Obtain the Freeze–Thaw Resistance of Concrete*; Instituto de Ciencias de la Construcción Eduardo Torroja: Madrid, Spain, 2015.
12. Haynack, A.; Timothy, J.J.; Kränkel, T.; Gehlen, C. Characterization of cementitious materials exposed to freezing and thawing in combination with de-icing salts using 3D scans. *Adv. Eng. Mater.* **2023**. . [CrossRef]
13. Powers, T.C. A working hypothesis for further studies of frost resistance of concrete. *Proc. J. Proc.* **1945**, *41*, 245–272.
14. Powers, T.C.; Helmuth, R. Theory of volume changes in hardened portland-cement paste during freezing. In *Highway Research Board Proceedings, Proceedings of the Thirty-Second Annual Meeting of the Highway Research Board, Washington, DC, USA, 13–16 January, 1953*; National Research Council, Highway Research Board: Washington, DC, USA, 1953; Volume 32.
15. BAŽANT, Z.P.; Chern, J.C.; Rosenberg, A.M.; Gaidis, J.M. Mathematical model for freeze–thaw durability of concrete. *J. Am. Ceram. Soc.* **1988**, *71*, 776–783. [CrossRef]
16. Zuber, B.; Marchand, J. Modeling the deterioration of hydrated cement systems exposed to frost action: Part 1: Description of the mathematical model. *Cem. Concr. Res.* **2000**, *30*, 1929–1939. [CrossRef]
17. Zuber, B.; Marchand, J. Predicting the volume instability of hydrated cement systems upon freezing using poro-mechanics and local phase equilibria. *Mater. Struct.* **2004**, *37*, 257–270. [CrossRef]
18. Yang, R.; Lemarchand, E.; Fen-Chong, T.; Azouni, A. A micromechanics model for partial freezing in porous media. *Int. J. Solids Struct.* **2015**, *75–76*, 109–121. [CrossRef]

19. Timothy, J.J.; Haynack, A.; Kränkel, T.; Gehlen, C. What Is the Internal Pressure That Initiates Damage in Cementitious Materials during Freezing and Thawing? A Micromechanical Analysis. *Appl. Mech.* **2022**, *3*, 1288–1298. [CrossRef]

20. Ožbolt, J. *MASA–Macroscopic Space Analysis*; Bericht zur Beschreibung des FE-Programmes MASA; Institut für Werkstoffe im Bauwesen, Universität Stuttgart: Stuttgart, Germany, 1998.

21. Ožbolt, J.; Li, Y.; Kožar, I. Microplane model for concrete with relaxed kinematic constraint. *Int. J. Solids Struct.* **2001**, *38*, 2683–2711. [CrossRef]

22. *DIN EN 197-1:2011-11*; Cement—Part 1: Composition, Specifications and Conformity Criteria for Common Cements; German Version EN 197-1:2011. Beuth Verlag: Berlin, Germany, 2011.

23. Zadran, S.; Ožbolt, J.; Gambarelli, S. Numerical analysis of freezing behaviour of saturated cementitious materials with different amounts of chloride. *Materials* **2023**.

24. Ožbolt, J.; Oršanić, F.; Balabanić, G. Modeling influence of hysteretic moisture behaviour on distribution of chlorides in concrete. *Cem. Concr. Compos.* **2016**, *67*, 73–84. [CrossRef]

25. Fagerlund, G. Critical Degrees of Saturation at Freezing of Porous and Brittle Materials. Ph.D. Thesis, Division of Building Materials, 1973.

26. Zeng, Q.; Li, K.; Fen-Chong, T.; Dangla, P. Effect of porosity on thermal expansion coefficient of cement pastes and mortars. *Constr. Build. Mater.* **2012**, *28*, 468–475. [CrossRef]

27. Li, K.; Xu, L.; Stroeven, P.; Shi, C. Water permeability of unsaturated cementitious materials: A review. *Constr. Build. Mater.* **2021**, *302*, 124168. [CrossRef]

28. Li, K.; Stroeven, P.; Stroeven, M.; Sluys, L. Liquid water permeability of partially saturated cement paste assessed by dem-based methodology. In Proceedings of the 11th International Symposium on Brittle Matrix Composites, BMC-11, Warsaw, Poland, 28–30 September 2015; Institute of Fundamental Technological Research PAS: Warsaw, Poland, 2015.

29. Washburn, E.W. The Dynamics of Capillary Flow. *Phys. Rev.* **1921**, *17*, 273–283. [CrossRef]

30. Canut, M. Pore Structure in Blended Cement Pastes. Ph.D. Thesis, Technical University of Denmark, Lyngby, Denmark, 2011.